

Cite this: *Nanoscale*, 2018, **10**, 1815

# Nanoscale chemical imaging of solid–liquid interfaces using tip-enhanced Raman spectroscopy†

 Naresh Kumar, <sup>a,b</sup> Weitao Su, <sup>c</sup> Martin Veselý,<sup>b</sup> Bert M. Weckhuysen, <sup>b</sup>  
 Andrew J. Pollard <sup>a</sup> and Andrew J. Wain <sup>\*a</sup>

Tip-enhanced Raman spectroscopy (TERS) is a powerful tool for non-destructive and label-free surface molecular mapping at the nanoscale. However, to date nanoscale resolution chemical imaging in a liquid environment has not been possible, in part due to the lack of robust TERS probes that are stable when immersed in a liquid. In this work, we have addressed this challenge by developing plasmonically-active TERS probes with a multilayer metal coating structure that can be successfully used within a liquid environment. Using these novel TERS probes, we have compared the plasmonic enhancement of TERS signals in air and water environments for both gap mode and non-gap mode configurations and show that in both cases the plasmonic enhancement decreases in water. To better understand the signal attenuation in water, we have performed numerical simulations that revealed a negative correlation between the electric field enhancement at the TERS probe-apex and the refractive index of the surrounding medium. Finally, using these robust probes we demonstrate TERS imaging with nanoscale spatial resolution in a water environment for the first time by employing single-wall carbon nanotubes as a model sample. Our findings are expected to broaden the scope of TERS to a range of scientific disciplines in which nanostructured solid–liquid interfaces play a key role.

Received 6th November 2017,  
Accepted 7th December 2017

DOI: 10.1039/c7nr08257f

rsc.li/nanoscale

## 1. Introduction

Understanding how the heterogeneity of nanostructured surfaces impacts their behaviour on the macroscopic scale plays a vital role in the design, development and implementation of new chemically functional materials. Surface analytical tools are indispensable in the characterisation of such materials, but often lack the desired spatiotemporal resolution and sensitivity to isolate the chemically distinctive features of interest, as well as determine their distribution. Moreover, many tech-

niques are not sufficiently adaptable to be implemented in an *in situ* or *operando* environment, which is critical for the identification of chemically active sites.<sup>1</sup> This need for versatility is particularly pertinent for solid–liquid interfaces, since the presence of a liquid phase in contact with the sample often hampers nanoscale characterisation. Such interfaces feature heavily in a wide range of scientific disciplines including heterogeneous catalysis,<sup>2</sup> electrochemistry<sup>3</sup> and biology,<sup>4</sup> in which mapping chemical behaviour presents a fundamental challenge.

Over the last decade and a half, tip-enhanced Raman spectroscopy (TERS) has emerged as a powerful nanoanalytical tool for simultaneous topographical and molecular mapping of surfaces at the nanoscale.<sup>5,6</sup> TERS operates on the principle of localised surface plasmon resonance (LSPR), whereby a high intensity electric field is generated at the apex of a metal or metal-coated scanning probe microscopy probe positioned at the focal point of an excitation laser,<sup>7</sup> as shown schematically in Fig. 1. The LSPR between the excitation laser and the metal nanoparticles at the probe-apex enhances the intensity of the electric field by several orders of magnitude and this enhancement is confined to a region similar to the size of the nanoparticles.<sup>7,8</sup> This effect simultaneously enhances the sensitivity and spatial resolution of Raman microscopy, pushing it beyond the diffraction limit. Since its first experimental

<sup>a</sup>National Physical Laboratory, Teddington, Middlesex, TW11 0LW, UK.  
E-mail: andy.wain@npl.co.uk

<sup>b</sup>Faculty of Science, Debye Institute for Nanomaterials Science, Utrecht University, Universiteitsweg 99, 3584 CG Utrecht, The Netherlands

<sup>c</sup>College of Materials and Environmental Engineering, Hangzhou Dianzi University, 310018 Hangzhou, China

†Electronic supplementary information (ESI) available: SEM images of TERS probes with different metal coatings before and after immersion in water; determination of TERS and far-field sampling volumes; time-series TERS spectra measured at a BPT SAM in air and water; correlation of TERS signal half-life with the excitation laser power; details of numerical simulation model; AFM topography image of the SWCNT sample and line profile analysis; TERS images of SWCNTs in air and water and estimation of their spatial resolution; lateral size of electric-field enhancement in air and water calculated using numerical simulations. See DOI: 10.1039/c7nr08257f

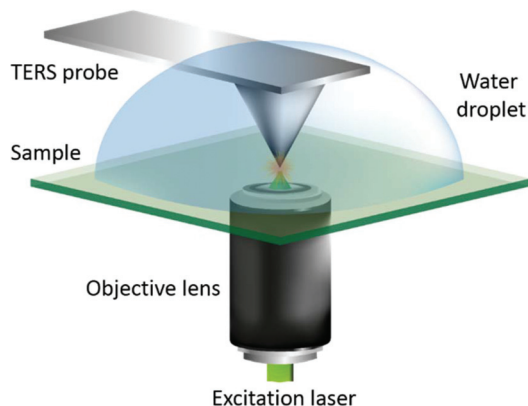


**Fig. 1** Schematic diagram of the AFM-TERS system employed. For TERS measurements in liquid, a water droplet was placed on the sample and measurements were performed with the TERS probe fully immersed.

demonstration in 2000,<sup>9–11</sup> TERS has been successfully used for nanoscale chemical characterisation in a wide range of research areas such as organic photovoltaic devices,<sup>12</sup> catalysis,<sup>13–15</sup> polymer-blends,<sup>16</sup> biological cells,<sup>17</sup> crystalline<sup>18</sup> and semiconductor<sup>19</sup> materials, graphene<sup>20,21</sup> and related two-dimensional (2D)<sup>22</sup> materials, single-wall carbon nanotubes (SWCNT)<sup>23</sup> and other one-dimensional<sup>24</sup> materials and single molecule mapping.<sup>25,26</sup> However, the majority of these studies have been performed in ambient air or ultrahigh vacuum<sup>27–29</sup> with only a few in aqueous,<sup>30–33</sup> organic liquid<sup>34</sup> and electrochemical<sup>35–39</sup> environments. Furthermore, TERS experiments in liquids have been almost exclusively restricted to point spectroscopy measurements and attempts at 2D chemical imaging in liquids have been met with very limited success. Maisonhaute *et al.* presented a TERS image of a self-assembled molecular monolayer on gold but the liquid-phase measurement was confined to a thin organic solvent layer, with only partial probe immersion.<sup>34</sup> Moreover, no defined spatial features could be resolved in the spectral map, highlighting the difficulty in generating meaningful 2D information using this technique.

One of the key challenges in generating TERS images in a liquid environment is the lack of robust plasmonically active probes. This is especially true for atomic force microscopy (AFM)-TERS, which offers the benefits of tapping- and contact-mode positional feedback, but typically relies on metal-coated probes which have been shown to exhibit rapid delamination when exposed to liquid.<sup>30</sup> This delamination issue precludes liquid phase TERS imaging due to the long measurement times associated with spectral acquisition at each pixel. To address the stability of TERS probes in liquids, Schmid *et al.*<sup>30</sup> and more recently Scherger and Foster<sup>32</sup> have reported the development of AFM-TERS probes using an adhesion layer of SiO<sub>x</sub> for Ag-coating or using titanium nitride coating with an alumina protective layer, respectively. In both cases the stability of the plasmonic coating was improved but physical degradation was still observed after exposure to water for 1–2 h and in neither case was chemical imaging demonstrated.

The majority of TERS studies in liquid environments to date have been carried out either in gap mode, where the sample is supported on a metal substrate (which benefits from additional signal enhancement due to electromagnetic coupling between surface plasmons in the metallic tip and the metal substrate) or in non-gap mode, where samples are supported on a dielectric substrate. To the best of our knowledge, a systematic comparison between TERS measurements in gap mode and non-gap mode within a liquid environment has never been reported and the impact of a liquid medium on the TERS signal enhancement across these two configurations has not been explored in detail.

In this work, we report the development of robust AFM-TERS probes, with a multilayer metal coating structure, that are highly stable and capable of performing successful TERS measurements in both air and liquid environments. Since the nature of the substrate has a major impact on the TERS enhancement factor, we demonstrate TERS measurements in water in both non-gap mode and gap mode. Non-resonant analyte molecules are investigated, with the TERS probe fully immersed in water and these results are then compared with equivalent measurements in air. Furthermore, to understand the differences in plasmonic enhancement in air and water, we have carried out numerical simulations of the electric field enhancement at the apex of the TERS probe in gap mode and non-gap mode configurations. Finally, using these robust probes, we demonstrate nanoscale TERS imaging of SWCNTs in a liquid environment in non-gap mode for the first time. This work paves the way for performing spatially resolved, *in situ* chemical characterisation at the nanoscale in a wide range of applications, which feature solid-liquid interfaces with nanoscale features.

## 2. Experimental details

### 2.1. TERS probe preparation

TERS probes with three different types of metal coating were prepared and tested for their stability in a liquid environment: (1) Ag coated TERS probes were prepared by oxidising commercial Si AFM cantilevers (CSC17/No Al, MikroMasch, USA) to a thickness of 300 nm SiO<sub>2</sub> and then depositing a 100 nm thick Ag layer using a vacuum evaporator (MB 200B, MBRAUN, Germany) at a pressure of 10<sup>−6</sup> mbar *via* thermal evaporation; (2) Cr-Ag coated TERS probes were prepared by depositing 3.5 nm Cr, followed by 100 nm Ag layers onto oxidised Si AFM cantilevers; (3) Cr-Au-Ag coated TERS probes were prepared by sequentially depositing 3.5 nm Cr, 10 nm Au and 100 nm Ag layers onto oxidised Si AFM cantilevers. Deposition rates of 0.02 nm s<sup>−1</sup>, 0.03 nm s<sup>−1</sup> and 0.05 nm s<sup>−1</sup> were used for the deposition of Cr, Au and Ag, respectively.

### 2.2. TERS set-up and measurements

Measurements were performed using a bespoke transmission-mode TERS system consisting of an AFM (Combiscope, AIST-NT, USA) secured on the top of an inverted confocal

optical microscope (Ti-U Eclipse, Nikon, Japan) attached to a Raman spectrometer (iHR 320, HORIBA Scientific, France) and a charge-coupled device detector (Newton, Andor, Ireland). A 532 nm excitation laser was radially-polarised and focused on the sample using a 1.49 NA, 100 $\times$  oil immersion microscope objective (Apo TIRF, Nikon, Japan) for all confocal Raman spectroscopy and TERS measurements. All TERS measurements were performed using contact-mode AFM feedback. Far-field measurements were conducted by retracting the TERS probe from the sample and refocusing the laser at the same spot on the sample. The intensity of Raman bands in the measured TERS and far-field spectra was calculated from the height of fitted Lorentzian peaks after linear background subtraction.

### 2.3. Sample preparation

Three different samples were investigated in this study:

(1) Polystyrene (PS) thin film samples for non-gap mode TERS measurements were prepared by spin-coating a 20 mg ml<sup>-1</sup> solution of PS (Sigma-Aldrich, USA) in chloroform onto 0.17 mm thick glass coverslips at 2000 revolutions per minute for 2 minutes.

(2) Biphenyl thiol (BPT) self-assembled monolayer (SAM) samples for gap mode TERS measurements were prepared by first depositing a 10 nm Au layer on glass coverslips *via* thermal evaporation. The Au-coated coverslips were then immersed in 5 mM solution of BPT (Sigma-Aldrich, USA) in ethanol for 18 h at 50 $^{\circ}$  C in order to form a densely-packed BPT SAM. Samples were rinsed in ethanol and deionised water to remove any physisorbed molecules from the sample surface.

(3) SWCNT samples were prepared for TERS imaging by depositing SWCNTs (NIST, USA) from a solution of 1% deoxycholate (DOC) onto piranha-cleaned (3-aminopropyl)triethoxysilane (APTES)-functionalised glass coverslips.

## 3. Results and discussion

### 3.1. Development of robust TERS probes

AFM-TERS probes are typically prepared by coating commercial Si AFM cantilevers with a thin film (20–100 nm) of Ag or Au. However, the plasmonic metal coating of such probes is not stable when exposed to an aqueous environment. Fig. 2a depicts a scanning electron microscopy (SEM) image of a typical Ag coated TERS probe and Fig. 2b shows an SEM image of a Ag probe after immersing in water for 1 h at room temperature. The Ag coating of the TERS probe exhibits evidence of severe localised corrosion and delamination after exposure to the aqueous environment. Loss of surface material and exposure of the underlying SiO<sub>2</sub> surface is clearly observed on the probe itself, as well as the cantilever, as shown in ESI Fig. S1a and S1b.<sup>†</sup>

To improve the stability of the Ag coating in water, we first tried an adhesion layer of 3.5 nm Cr between the SiO<sub>2</sub> and the 100 nm Ag coating. Fig. 2c and d show SEM images of a Cr–Ag coated TERS before and after immersion in water for 1 h.

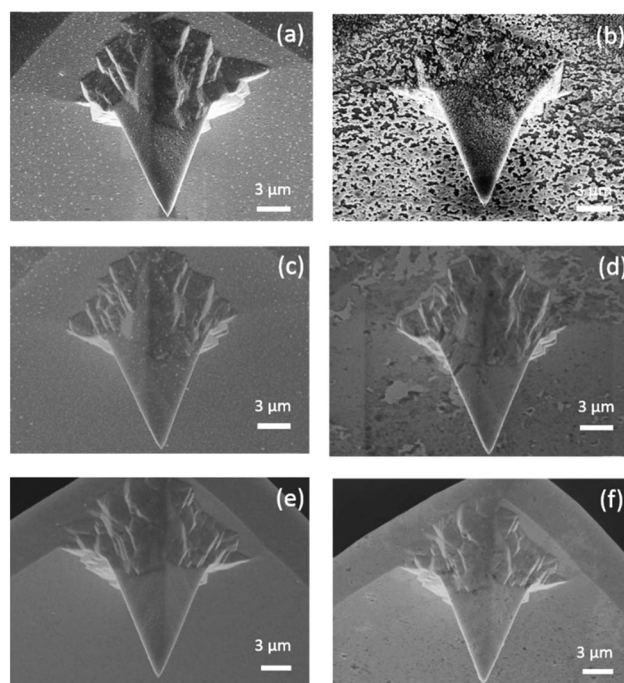


**Fig. 2** SEM images of a Ag coated TERS probe (a) before and (b) after immersing in water for 1 h. SEM image of a Cr–Ag coated TERS probe (c) before and (d) after immersing in water for 1 h. SEM image of a Cr–Au–Ag coated TERS probe (e) before and (f) after immersing in water for 1 h.

Although the adhesion of the Ag coating is improved for the Cr–Ag probe compared to the Ag-only coated probe, the coating still undergoes degradation. Parts of the Ag-coating are lost from several regions of the probe shaft as well as the cantilever (see ESI Fig. S1c and S1d<sup>†</sup>).

Finally, we used a 10 nm buffer layer of Au between the Cr and Ag layers, since Cr and Au are well known to exhibit very strong adhesion.<sup>40,41</sup> Fig. 2e and f show the SEM images of Cr–Au–Ag coated probes before and after immersion in water for 1 h. In this case, the metal coating of the TERS probe shows no evidence of degradation on the probe shaft or the cantilever (see ESI Fig. S1e and S1f<sup>†</sup>). SEM images of two additional Cr–Au–Ag coated TERS probes before and after immersion in water for 1 h are presented in ESI Fig. S2,<sup>†</sup> showing complete preservation of Ag coating after exposure to the aqueous environment. The significant improvement in water-resistance of the Cr–Au–Ag coated probes likely relates to the improved continuity of the Ag coating which we speculate results from the improved adhesion between Ag and Au compared to Ag and Cr. The SEM image of the Ag-coated TERS probe cantilever in ESI Fig. S1<sup>†</sup> shows that the Ag coating is rather inhomogeneous and contains a significant number of pinholes. This can expose the underlying SiO<sub>2</sub> surface to water, leaving the Ag layer susceptible to oxidation and delamination from the underside. In contrast, the Cr–Ag and Cr–Au–Ag probes (ESI Fig. S1c and S1e<sup>†</sup>) show a progressive improvement in the uniformity of the Ag coating, which correlates with the corres-



ponding improvement in their water resistance. Given their high stability in water, all TERS measurements in this study were performed using Cr–Au–Ag coated TERS probes.

### 3.2. Comparison of TERS plasmonic enhancement in air and water

To compare the TERS plasmonic enhancement in air and water we performed TERS measurements in non-gap mode and gap mode configurations using the Cr–Au–Ag coated TERS probes. Non-gap mode TERS measurements were performed on a thin film of PS on a glass substrate. The thickness of the PS film was estimated to be of the order of 100 nm, based on AFM measurements (ESI Fig. S3†). Spectra measured with the TERS probe in contact with the sample (TERS) and retracted from the sample (far-field) in air are presented in Fig. 3a. The spectra are consistent with previous reports,<sup>16,42</sup> with intense bands at 1002 cm<sup>−1</sup> and 1602 cm<sup>−1</sup> attributed to the ring breathing mode and C=C stretch ( $\nu(\text{C}=\text{C})$ ) of the PS aromatic ring, respectively. The intensity of these bands is higher in the TERS measurement than in the far-field, as expected, due to

the plasmonic local electric field enhancement. Note that the TERS spectrum represents the sum of Raman intensity generated in the near-field (plasmonically-enhanced electric-field region at the TERS probe apex) as well as the far-field.

To quantify the enhancement factor (EF) of a Raman band due to the TERS effect we use the following equation:<sup>43</sup>

$$\text{EF} = \left( \frac{I_{\text{TERS}}}{I_{\text{FF}}} - 1 \right) \frac{V_{\text{FF}}}{V_{\text{NF}}} \quad (1)$$

where,  $I_{\text{TERS}}$  and  $I_{\text{FF}}$  are the intensity of a Raman band with the TERS probe in contact and retracted from the sample respectively.  $V_{\text{NF}}$  and  $V_{\text{FF}}$  are the sampling volumes associated with the near-field and far-field measurements, respectively. See ESI Fig. S3† for details of how  $V_{\text{NF}}$  and  $V_{\text{FF}}$  were estimated in this work. Using eqn (1), the EF of TERS signals with three nominally identical probes in air was calculated using the intensity of the 1602 cm<sup>−1</sup> band to be  $8.6 \pm 2.5 \times 10^3$ , where the uncertainty is the standard deviation. This band was chosen for the EF calculation to facilitate comparison with the gap mode measurements below, in which the same aromatic vibrational mode is excited.

Next, TERS measurements of the PS thin film were performed in a liquid environment by placing a water droplet on the sample surface and fully immersing the TERS probe inside the droplet as illustrated in Fig. 1. The resulting TERS and far-field spectra are depicted in Fig. 3b. In water, the far-field signal intensity of the 1602 cm<sup>−1</sup> band was found to decrease by a factor of  $3.5 \pm 1.2$  compared to air. This is similar to the attenuation reported by Sabanés *et al.*,<sup>33</sup> who attributed the loss in intensity to a distortion of laser focus resulting from the presence of water on the sample. The loss of optical coupling most likely originates from a combination of laser focus distortion and dielectric loss of laser field intensity due to the higher refractive index (RI) of water compared to air (see discussion in the next section). However, since the EF in eqn (1) is determined from the ratio of the TERS and far-field signal intensity, our calculation of EF should not be affected by the decrease of optical coupling in water. In water, the EF of the 1602 cm<sup>−1</sup> Raman band was estimated to be  $6.0 \pm 3.4 \times 10^3$ , showing a slight reduction of the mean EF by a factor of  $1.4 \pm 0.9$  compared to air. Comparable behaviour was also observed for the 1002 cm<sup>−1</sup> band. The similarity of TERS EF measured in air and water indicates that, despite the decrease in optical coupling discussed above, TERS probes undergo efficient LSPR with the excitation laser in water.

To compare the plasmonic enhancement in air and water in gap mode, we carried out TERS measurements on a BPT SAM formed on a 10 nm thick Au film on a glass substrate. Fig. 3c shows TERS and far-field spectra measured on the BPT SAM in air. In the far-field, no Raman bands are observed in the spectrum because the sensitivity of confocal Raman spectroscopy is too low to produce a detectable signal from a monolayer of BPT molecules present. This is consistent with the previously reported far-field measurements of SAMs of organic molecules adsorbed on Au.<sup>30,33,34</sup> However, in the

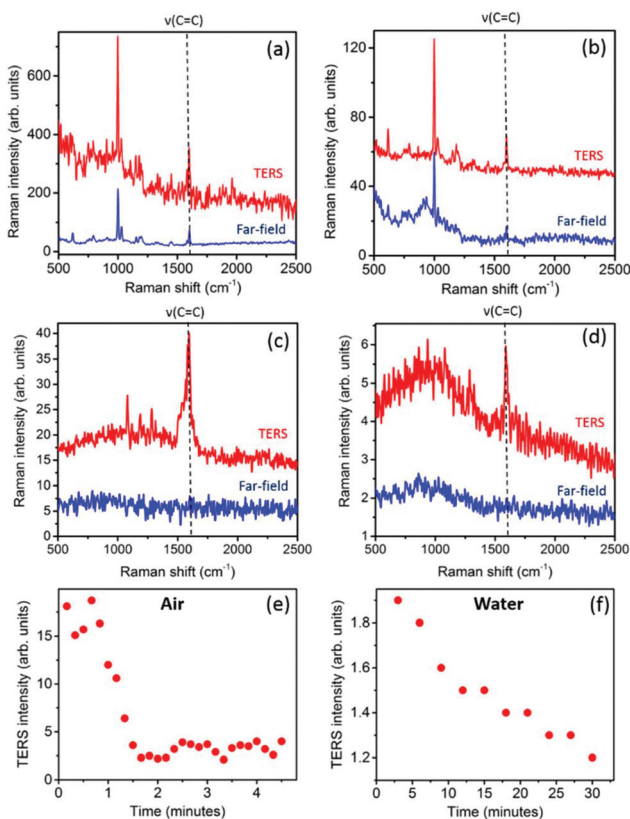


**Fig. 3** TERS and far-field Raman spectra of a PS thin film on glass in (a) air and (b) water. Integration time: 60 s, laser power at the sample: 170  $\mu\text{W}$ . TERS and far-field spectra of a BPT SAM on a Au substrate in (c) air and (d) water. Integration time: 1 s in air, 60 s in water, laser power at the sample: 117  $\mu\text{W}$ . Typical plots of the 1593 cm<sup>−1</sup> band intensity versus time for BPT TERS signal in (e) air (integration time: 1 s) and (f) water (integration time: 60 s). The TERS and far-field spectra measured for the BPT SAMs in water have been normalised by integration time for comparison with the corresponding measurements in air.

TERS spectrum, due to the strong plasmonic enhancement of the electric field at the TERS probe-apex, the characteristic BPT Raman bands at  $1081\text{ cm}^{-1}$  ( $\delta(\text{C-H})$ ),  $1285\text{ cm}^{-1}$  ( $\nu(\text{C=C})$ ) and  $1593\text{ cm}^{-1}$  ( $\nu(\text{C=C})$ ) become clearly visible.<sup>44,45</sup>

The TERS and far-field Raman spectra from the BPT SAM sample measured in water are shown in Fig. 3d. Similar to the measurements in air, no Raman bands are observed in the far-field spectrum measured in water, whereas the characteristic BPT Raman bands appear in the TERS spectrum. However, the TERS signal intensity is significantly reduced in water compared to air such that only the BPT Raman band at  $1593\text{ cm}^{-1}$  is clearly visible in the TERS spectrum. The average TERS intensity of the  $1593\text{ cm}^{-1}$  BPT Raman band measured using three nominally identical probes was found to decrease by an order of magnitude from  $15 \pm 5$  (arb. units) in air to  $1.5 \pm 0.4$  (arb. units) in water. This reduction in signal intensity in water compared to air is comparable to previous reports of STM-TERS measurements on a thiophenol SAM, a similar non-resonant probe molecule.<sup>33</sup> Furthermore, the signal to noise ratio (SNR) of the same TERS band also decreases from  $13 \pm 1$  in air to  $4.7 \pm 0.1$  in water, where the noise level was determined from the standard deviation of TERS intensity between  $1710\text{ cm}^{-1}$  and  $2500\text{ cm}^{-1}$ . This suggests a significant loss in TERS sensitivity in water compared to air. Interestingly, although no Raman bands were observed in the far-field, the noise level in the far-field spectra, calculated from the standard deviation of Raman intensity between  $1470\text{ cm}^{-1}$  and  $1670\text{ cm}^{-1}$ , was found to decrease by a factor of  $10 \pm 1$  in water compared to air. Comparison of this with the factor of 3.6 calculated above for the PS film measurements suggests that the far-field optical losses associated with water in gap mode are about three times higher than in non-gap mode.

Since no BPT Raman bands are observed in the far-field, it is not possible to calculate the EF for the TERS measurements in Fig. 3c and d using eqn (1). However, it is possible to estimate a minimum value of the EF by assuming that the intensity of the  $1593\text{ cm}^{-1}$  BPT Raman band in the far-field is at most equal to the noise level in the same spectral range. In the case of a molecular monolayer, the near-field and far-field sampling volumes in eqn (1) may be approximated by the respective probe areas at the sample surface.<sup>43</sup> These probe areas can be estimated from the diameter of the TERS probe-apex ( $\approx 40\text{ nm}$ ) measured using SEM imaging (see ESI Fig. 3c†) and the excitation laser spot size ( $\approx 450\text{ nm}$ ), respectively.<sup>30,43</sup> Using this approach, the minimum EF of the  $1593\text{ cm}^{-1}$  BPT Raman band is estimated to be  $1.1 \pm 0.4 \times 10^3$  and  $1.1 \pm 0.3 \times 10^3$  in air and water, respectively. The similarity in these minimum EF values indicates that the loss in near-field sensitivity in water evidenced by the decrease in SNR, is compensated for by the decrease in far field intensity resulting from the optical losses discussed above. This use of minimum EFs should be treated with caution, however, since their calculation is clearly complicated by varying noise levels between air and water. For ease of comparison, the EF and SNR values estimated from the gap mode measurements are summarised in Table 1, along with the EF values for non-gap mode.

**Table 1** Summary of TERS EF values for gap mode and non-gap mode in air and water estimated from experimental data and comparison with electric field enhancement data obtained from numerical simulations

Experimental measurement of TERS EF		
	Non-gap mode EF	Gap mode minimum EF (TERS SNR)
Air	$8.6 \pm 2.5 \times 10^3$	$1.1 \pm 0.4 \times 10^3$ ( $13 \pm 1$ )
Water	$6.0 \pm 3.4 \times 10^3$	$1.1 \pm 0.3 \times 10^3$ ( $4.7 \pm 0.1$ )
Air : water ratio	$1.4 \pm 0.9$	$1 \pm 0.5$ ( $2.8 \pm 0.2$ )
Numerical simulations of electric field enhancement		
	Non-gap mode	Gap mode
Air	5.3	1875.2
Water	2.7	453.3
Air : water ratio	1.9	4.1

An additional observation evident from time-series TERS measurements in gap mode was that the signal intensity from the BPT SAM was found to decay in air as shown in Fig. 3e. See ESI Fig. S4a† for the corresponding time-series TERS spectra. The  $1593\text{ cm}^{-1}$  band intensity decreased to 50% of its initial value (*i.e.* the half-life) within approximately 2 minutes, based on average TERS measurements from three nominally identical TERS tips. In contrast, whilst the absolute TERS signal intensity was suppressed by the presence of water, it was found to decay much more slowly in this environment, with a corresponding half-life of  $>30$  minutes (see Fig. 3f and ESI Fig. S4b†). We propose that the rapid decrease in TERS signal in air arises from thermal degradation of the BPT SAM in the TERS near-field, possibly through molecular desorption under the intense electric field, which may increase the local temperature by up to  $50^\circ\text{C}$ .<sup>27,46</sup> Such a heating effect from LSPR has been previously shown to cause desorption of analyte molecules in surface-enhanced Raman spectroscopy (SERS) measurements leading to complete loss of signal intensity.<sup>47</sup> The presence of water not only decreases the electric field enhancement, but is also expected to act as a heat sink, improving heat dissipation through thermal conduction.<sup>30,48</sup> Consistent with this theory, the half life of the TERS signal decay in air was found to be negatively correlated with excitation laser power, as shown in ESI Fig. S5.†

### 3.3. Numerical simulations of electric field enhancement in air and water

To better understand the observed differences in plasmonic enhancement in gap mode and non-gap mode TERS configurations, we performed numerical simulations using finite-element modelling in Comsol Multiphysics®. A model of the TERS probes with a multilayer coating of  $3.5\text{ nm Cr}$ ,  $10\text{ nm Au}$  and  $100\text{ nm Ag}$ , as used in this study, was constructed. The electric field enhancement was calculated at the TERS probe-apex in non-gap mode (glass substrate) and gap mode ( $10\text{ nm Au}$  on a glass substrate) in both air and water environments. See ESI Fig. S6† for further details of the simulation model.

Fig. 4a and b show simulated maps of the electric field enhancement surrounding a TERS probe on a glass substrate (non-gap mode) in air and water, respectively. Electric field enhancement is defined as  $E/E_0$ , where  $E$  is the amplitude of electric field at the substrate (beneath the probe apex) with the TERS probe present and  $E_0$  is the electric field amplitude ( $= 1$ ) at the substrate without the TERS probe. The calculated enhancement is found to be 1.9 times greater in air compared to water. This is consistent with the experimental results presented in the previous section where the mean EF of PS TERS signals decreased by a factor of 1.4 in water compared to air.

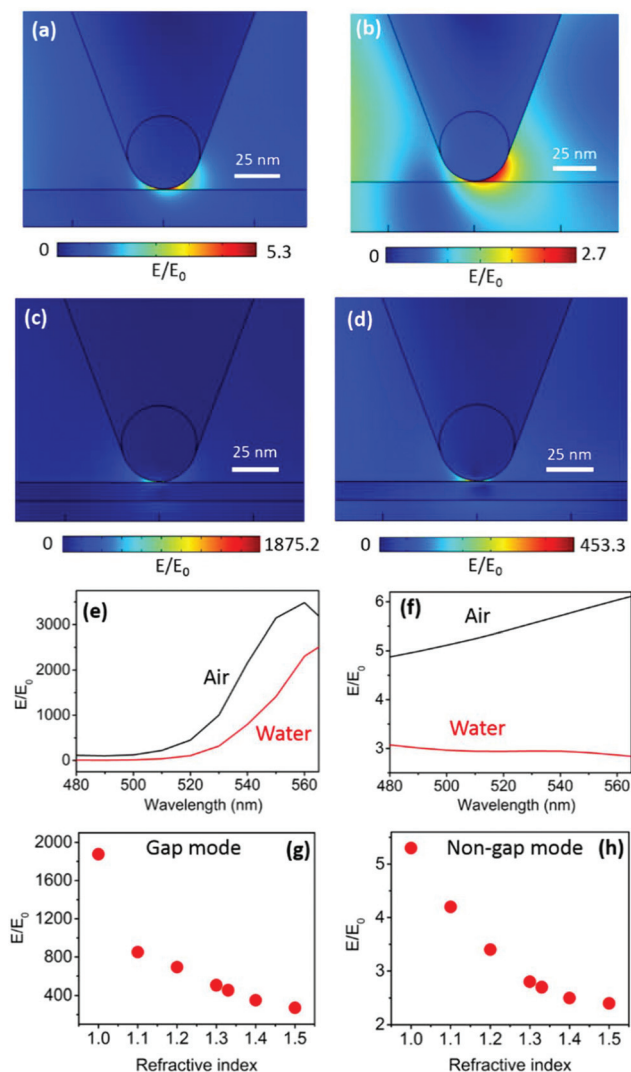


**Fig. 4** Numerical simulation maps of the electric field enhancement at the apex of a modelled TERS probe in contact with a glass coverslip (non-gap mode) in (a) air and in (b) water. Numerical simulation maps of electric field enhancement at the apex of a modelled TERS probe in contact with a 10 nm Au film on glass (gap mode) in (c) air and in (d) water. Plots of calculated electric field enhancement at the probe-apex versus excitation laser wavelength in (e) gap mode and (f) non-gap mode. Variation of calculated electric field enhancement with RI of the surrounding medium at the probe-apex in (g) gap mode and (h) non-gap mode.

Equivalent electric field enhancement simulations for a TERS probe on 10 nm Au film (gap mode) in air and water are shown in Fig. 4c and d, respectively. The calculated enhancement is clearly greater in air compared to water but in both cases is spatially localised to the contact point between the probe apex and the sample. A quantitative comparison of the calculated electric field enhancement in air and water is presented in Table 1, along with the relevant experimental values discussed in the previous section. The maximum electric field enhancement in gap mode determined through simulations is found to be 4.1 times higher in air than water, indicating a stronger TERS enhancement in air. This is consistent with our experimental observation of a lower TERS sensitivity for measurements of the BPT SAM on Au in water discussed in the previous section. Although the EF of TERS measurements in gap mode cannot be precisely determined due to unobservable Raman bands in the far-field spectra (see discussion above), the SNR of the TERS signal, presented in parentheses in Table 1, decreased by about 2.8 times in water compared to air, indicating a much lower electric field enhancement at the TERS probe-apex.

The simulation results show that the maximum electric field enhancement in non-gap mode (Fig. 4a and b) is approximately three orders of magnitude smaller than gap mode in both air and water (Fig. 4c and d), which is consistent with experimental results reported previously.<sup>49</sup> Furthermore, across the entire green light wavelength range (520 nm–560 nm)<sup>50</sup> a higher electric field enhancement is revealed in air compared to water in both gap mode and non-gap mode, as shown in Fig. 4e and f, respectively. It is interesting to note that the decrease in the electric field enhancement from air to water was found to be smaller in non-gap mode (a factor of 1.9) compared to gap mode (a factor of 4.1). However, since an accurate calculation of EF cannot be achieved from our gap mode TERS data, this trend could not be verified experimentally.

To gain further insights into the decrease of the electric field enhancement in water compared to air, we calculated the electric field enhancement at the TERS probe-apex as a function of the RI of the surrounding medium. The electric field enhancement was found to decrease with increasing RI in both gap mode and non-gap mode as shown in Fig. 4g and h. Furthermore, a sharper drop in electric field enhancement with increasing RI is observed in gap mode compared to non-gap mode. These simulation results are consistent with previous experimental reports in which the LSPR of Ag and Au nanoparticles was found to red-shift with an increase in local RI.<sup>51–53</sup> For Ag, the LSPR was observed to shift by up to 35 nm per 0.1 RI increase.<sup>51</sup> Since we used a 532 nm excitation laser, a red-shift of the LSPR in water (RI = 1.33) compared to air (RI = 1) would lead to a loss in electric field enhancement and hence a decrease in TERS EF as observed *via* numerical simulations and TERS experiments in our study. This relationship between electric field enhancement and RI may also offer a physical rationale for the loss of TERS sensitivity observed experimentally in water compared to air, in that the presence



of a higher dielectric medium results in near-field optical losses due to dipolar interactions at the probe–substrate interface. Given the additional plasmonic enhancement associated with the gold surface in gap mode, it is not surprising that the above attenuation is more pronounced in this configuration.

Note that our simulation model greatly simplifies the real TERS experimental conditions, for example by ignoring the roughness of the Ag coating on TERS probes and the radial polarisation of the excitation laser incident onto the underside of the sample in a bottom-up illumination geometry. It is also prudent to highlight the large uncertainties associated with the experimentally determined values of EF values presented in Table 1, which reflect the fact that nominally identical probes exhibit significantly different properties at the nanostructured apex. Nevertheless, the simulation results exhibit the same general trend as observed experimentally for the plasmonic signal enhancement, for both gap mode and non-gap mode, suggesting a reasonable agreement between experiment and theory.

### 3.4. Nanoscale Raman imaging in a liquid environment

Finally, we performed TERS imaging in air and water using Cr–Au–Ag coated TERS probes in order to critically compare their chemical imaging characteristics in these two environments. We used a glass coverslip decorated with SWCNTs for this purpose since the 1D nature of SWCNTs makes them convenient model structures to demonstrate high resolution imaging.<sup>54–56</sup> A line profile across the TERS image of a SWCNT gives a direct estimate of the size of the near-field enhancement area at the TERS probe–apex<sup>57</sup> and the spatial resolution achieved during the imaging.<sup>58</sup> We note there are different interpretations of the term “spatial resolution”; for simplicity we define it here as the full width at half maximum (FWHM) of the Raman signal intensity measured over a single 1D feature. Since the lateral dimensions of the SWCNT are significantly smaller than the probe apex dimensions, the spatial resolution is governed largely by the latter. Fig. 5a shows an AFM topography image of SWCNTs dispersed on a glass substrate. ESI Fig. S7† contains further AFM topography data for the same area. The height profiles of SWCNTs confirm that the carbon nanotubes are indeed single-walled and are singly distributed over the sample surface. Fig. 5b shows the confocal Raman spectrum of the SWCNT sample which exhibits the characteristic D, G and 2D Raman bands. A high-resolution TERS image of the G-band intensity (at  $1591\text{ cm}^{-1}$ ) for a SWCNT measured in air with a pixel size of 10 nm is shown in Fig. 5c. The G-band intensity at each pixel was determined from the height of a Lorentzian fit to the TERS spectrum in the  $1470\text{ cm}^{-1}$ – $1671\text{ cm}^{-1}$  spectral range after linear background subtraction using a MATLAB program. To minimize fitting errors, only the pixels in which the Raman intensity was at least three times higher than the median noise level in the chosen spectral range were fitted using a Lorentzian curve. To calculate the spatial resolution of the SWCNT TERS image in Fig. 5c, we used the procedure reported by Roy *et al.*,<sup>57</sup> which separates the near-field and far-field components in an inten-

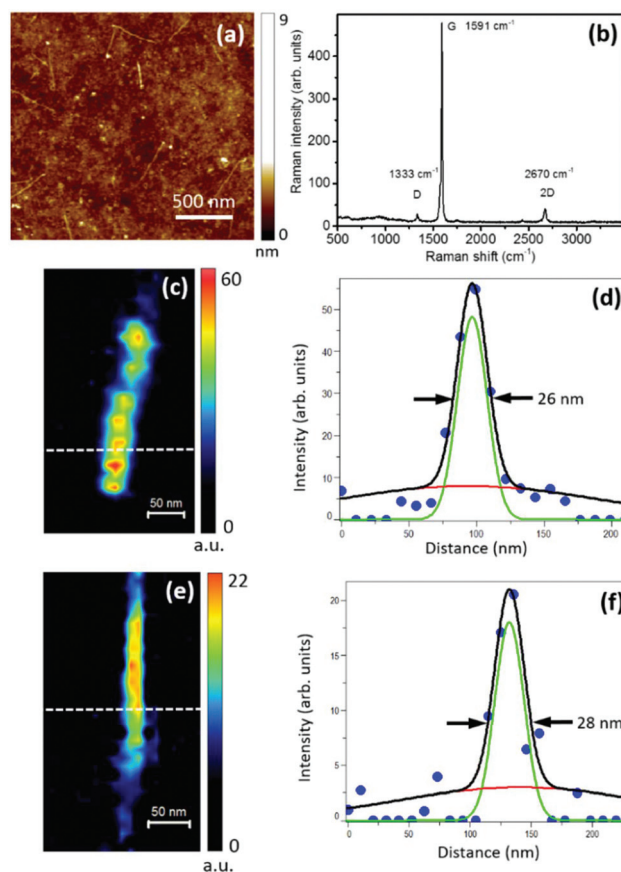


**Fig. 5** (a) AFM topography image showing distribution of SWCNTs over a glass substrate. (b) Confocal Raman spectrum of SWCNT sample. Integration time: 10 s. (c) TERS image of a SWCNT in air, obtained using the  $1591\text{ cm}^{-1}$  Raman band intensity. (d) Intensity profile along the line marked in (c) indicating Gaussian curves fits to the near-field (green) and far-field (red) contributions. (e) TERS image of a SWCNT in water, obtained using the  $1591\text{ cm}^{-1}$  Raman band intensity. (f) Intensity profile along the line marked in (e) with Gaussian curve fits. Integration time for TERS imaging: 1 s; nominal pixel size: 10 nm; laser power at the sample:  $170\text{ }\mu\text{W}$ .

sity profile measured across the TERS image of a SWCNT through fitting it with two different Gaussian curves. Fig. 5d shows an intensity profile across the line marked in Fig. 5c fitted with two Gaussian curves for the far-field (red) and near-field (green) contributions. The FWHM of the far-field Gaussian curve was set to 225 nm corresponding to a laser spot size of 450 nm. The near-field spatial resolution was estimated from the FWHM of the green Gaussian curve in Fig. 5d, to be  $\approx 26\text{ nm}$ .

We then performed TERS imaging of a SWCNT on the same sample immersed in water with 10 nm pixel size, an example of which is shown in Fig. 5e. Analysis of the corresponding line profile depicted in Fig. 5f gives an estimated spatial resolution of  $\approx 28\text{ nm}$ . Both TERS images exhibit intensity fluctuations along the length of the SWCNT, so in order to gain a more representative estimation of the spatial resolution in the two images shown, we performed the same fitting procedure

on three different line profiles across the TERS images in Fig. 5c and e and estimated the average spatial resolution in air and water to be  $28 \pm 2$  nm and  $26 \pm 2$  nm, respectively. See ESI Fig. S8† for full details of the analysis.

In order to gain a more statistical view of the performance of the TERS probes we performed imaging at several different areas on the SWCNT sample in air and water. The TERS images and corresponding analysis are presented in ESI Fig. S9 and S10† and a summary of the calculated spatial resolution data is presented in Table 2 and ESI Table S1.† The TERS images of SWCNTs in air exhibited an average spatial resolution ranging between 22 nm–28 nm. However, TERS imaging of SWCNTs was generally found to be more challenging in water than in air. In particular, the SWCNTs appeared to be displaced by the TERS probe during imaging, whereas the SWCNTs remained stationary whilst imaging in air, suggesting a weaker interaction between the SWCNTs and the substrate in water. Despite this difficulty we successfully obtained TERS images of SWCNTs in water with a spatial resolution ranging from 22 nm–62 nm. Although on average a poorer resolution was achieved in water, the difference between air and water is relatively small compared to the uncertainty in measurement. Indeed, the significantly wider spread of spatial resolution data across the water measurements reflects the practical difficulties encountered whilst performing TERS imaging in water, which may exacerbate the natural variation in imaging performance expected between TERS probes. It is also important to note that the pixel size used for the image presented in Fig. S10d† is larger than the estimated spatial resolution, so this value should be treated with caution as the Nyquist sampling criterion is not satisfied in this case. Nevertheless, these results clearly demonstrate the feasibility of spatially-resolved TERS measurements in liquid at nanometre length-scales using multi-layer metal-coated TERS probes.

The spatial resolution estimated from these TERS images is also consistent with the lateral size of the electric field enhancement calculated from the numerical simulation maps in non-gap mode for air and water (Fig. 4a and b). Horizontal line profiles across these maps (beneath the probe-apex) are shown along with Gaussian curve fits in ESI Fig. S11,† from which the lateral dimensions of the electric field enhancement can be estimated from the FWHM. A similar FWHM of Gaussian fits to the line profiles in air (21 nm) and water

(28 nm) suggests that although the electric field enhancement decreased in water, it remains confined to the TERS probe-apex. This also indicates that a similar lateral resolution for TERS imaging should be possible in both air and water, which is indeed substantiated by our experimental results.

## 4. Conclusions

In this work, we have developed robust plasmonically-active TERS probes capable of performing TERS imaging when fully immersed in a liquid environment. Using these novel probes, we have performed TERS measurements in water in both gap mode and non-gap mode configurations and analysed the difference in plasmonic enhancement of Raman signals with the corresponding measurements in air. Plasmonic enhancement was found to decrease in an aqueous environment compared to air in both gap mode and non-gap mode. Numerical simulations of the near-field intensity revealed a negative correlation between electric field enhancement at the TERS probe-apex and the RI of the surrounding medium, providing a physical basis for these experimental observations. Finally, we have demonstrated sub-30 nm resolution chemical imaging in a liquid environment using TERS for the first time. It has been shown that the TERS spatial resolution for SWCNTs measured in water can be similar to that observed in air, although experimental challenges in liquid lead to increased experimental variability. This work is expected to significantly broaden the potential application of AFM-TERS across scientific disciplines such as heterogeneous catalysis, electrochemistry and cellular biology, wherein non-destructive and label-free chemical mapping of nanostructured solid-liquid interfaces presents a key measurement challenge.

## Conflicts of interest

There are no conflicts of interest to declare.

## Acknowledgements

NK, AJP and AJW acknowledge funding from the National Measurement System of the UK Department of Business, Energy & Industry Strategy. WS acknowledges funding from Zhejiang Provincial Science foundation (Grant no. LY18F040006). MV acknowledges support from the NWO VIDI Grant No. 723.015.007. BMW acknowledges funding from a European Research Council (ERC) Advanced Grant (No. 321140) and a NWO Gravitation program, the Netherlands Center for Multiscale Catalytic Energy Conversion (MCEC). We also thank Dr Dario Imbraguglio from INRIM, Italy for providing SWCNT sample and Dr Sebastian Wood from NPL, UK for insightful discussions.

**Table 2** Comparison of the spatial resolution of SWCNT TERS images measured in air and water

	TERS image (pixel size/nm)	Spatial resolution/nm
Air	Fig. S8a (10)	$28 \pm 2$
	Fig. S9a (10)	$22 \pm 5$
	Fig. S9e (17)	$27 \pm 4$
Water	Fig. S8e (10)	$26 \pm 2$
	Fig. S10a (10)	$22 \pm 4$
	Fig. S10d (50)	$47 \pm 11$
	Fig. S10h (40)	$62 \pm 16$



## References

- I. L. C. Buurmans and B. M. Weckhuysen, *Nat. Chem.*, 2012, **4**, 873–886.
- B. M. Weckhuysen, *In-situ spectroscopy of catalysts*, American Scientific Publishers, Stevenson Ranch, CA, 2004.
- M. J. Weaver and X. Gao, *Annu. Rev. Phys. Chem.*, 1993, **44**, 459–494.
- Y. F. Dufrêne, *Nat. Rev. Microbiol.*, 2004, **2**, 451–460.
- T. Deckert-Gaudig, A. Taguchi, S. Kawata and V. Deckert, *Chem. Soc. Rev.*, 2017, **46**, 4077–4110.
- N. Kumar, S. Mignuzzi, W. Su and D. Roy, *EPJ Tech. Instrum.*, 2015, **2**, 9.
- P. Verma, *Chem. Rev.*, 2017, **117**, 6447–6466.
- A. Hartschuh, *Angew. Chem., Int. Ed.*, 2008, **47**, 8178–8191.
- R. M. Stockle, Y. D. Suh, V. Deckert and R. Zenobi, *Chem. Phys. Lett.*, 2000, **318**, 131–136.
- N. Hayazawa, Y. Inouye, Z. Sekkat and S. Kawata, *Opt. Commun.*, 2000, **183**, 333–336.
- M. S. Anderson, *Appl. Phys. Lett.*, 2000, **76**, 3130–3132.
- N. Kumar, A. Zoladek-Lemanczyk, A. A. Guilbert, W. Su, S. M. Tuladhar, T. Kirchartz, B. C. Schroeder, I. McCulloch, J. Nelson and D. Roy, *Nanoscale*, 2017, **9**, 2723–2731.
- E. M. van Schroyen Lantman, T. Deckert-Gaudig, A. J. G. Mank, V. Deckert and B. M. Weckhuysen, *Nat. Nanotechnol.*, 2012, **7**, 583–586.
- N. Kumar, B. Stephanidis, R. Zenobi, A. Wain and D. Roy, *Nanoscale*, 2015, **7**, 7133–7137.
- J.-H. Zhong, X. Jin, L. Meng, X. Wang, H.-S. Su, Z.-L. Yang, C. T. Williams and B. Ren, *Nat. Nanotechnol.*, 2017, **12**, 132–136.
- B. S. Yeo, E. Amstad, T. Schmid, J. Stadler and R. Zenobi, *Small*, 2009, **5**, 952–960.
- N. Kumar, M. M. Drozd, H. Jiang, D. M. Santos and D. J. Vaux, *Chem. Commun.*, 2017, **53**, 2451–2454.
- S. Berweger, C. C. Neacsu, Y. Mao, H. Zhou, S. S. Wong and M. B. Raschke, *Nat. Nanotechnol.*, 2009, **4**, 496–499.
- A. Lucia, O. A. Cacioppo, E. Iulianella, L. Latessa, G. Moccia, D. Passeri and M. Rossi, *Appl. Phys. Lett.*, 2017, **110**, 103105.
- S. Mignuzzi, N. Kumar, B. Brennan, I. S. Gilmore, D. Richards, A. J. Pollard and D. Roy, *Nanoscale*, 2015, **7**, 19413–19418.
- W. Su, N. Kumar, N. Dai and D. Roy, *Chem. Commun.*, 2016, **52**, 8227–8230.
- W. Su, N. Kumar, S. Mignuzzi, J. Crain and D. Roy, *Nanoscale*, 2016, **8**, 10564–10569.
- Y. Okuno, Y. Saito, S. Kawata and P. Verma, *Phys. Rev. Lett.*, 2013, **111**, 216101.
- M. Boehmler, Z. Wang, A. Myalitsin, A. Mews and A. Hartschuh, *Angew. Chem., Int. Ed.*, 2011, **50**, 11536–11538.
- R. Zhang, Y. Zhang, Z. C. Dong, S. Jiang, C. Zhang, L. G. Chen, L. Zhang, Y. Liao, J. Aizpurua, Y. Luo, J. L. Yang and J. G. Hou, *Nature*, 2013, **498**, 82–86.
- A. B. Zrimsek, N. Chiang, M. Mattei, S. Zaleski, M. O. McAnally, C. T. Chapman, A.-I. Henry, G. C. Schatz and R. P. Van Duyne, *Chem. Rev.*, 2016, **117**, 7583–7613.
- M. Sun, Z. Zhang, H. Zheng and H. Xu, *Sci. Rep.*, 2012, **2**, 647.
- E. A. Pozzi, M. D. Sonntag, N. Jiang, N. Chiang, T. Seideman, M. C. Hersam and R. P. Van Duyne, *J. Phys. Chem. Lett.*, 2014, **5**, 2657–2661.
- E. A. Pozzi, G. Goubert, N. Chiang, N. Jiang, C. T. Chapman, M. O. McAnally, A.-I. Henry, T. Seideman, G. C. Schatz and M. C. Hersam, *Chem. Rev.*, 2016, **117**, 4961–4982.
- T. Schmid, B. S. Yeo, G. Leong, J. Stadler and R. Zenobi, *J. Raman Spectrosc.*, 2009, **40**, 1392–1399.
- A. Nakata, T. Nomoto, T. Toyota and M. Fujinami, *Anal. Sci.*, 2013, **29**, 865–869.
- J. D. Scherger and M. D. Foster, *Langmuir*, 2017, **33**, 7818–7825.
- N. Martín Sabanés, L. M. Driessen and K. F. Domke, *Anal. Chem.*, 2016, **88**, 7108–7114.
- T. Touzalin, A. L. Dauphin, S. Joiret, I. T. Lucas and E. Maisonhaute, *Phys. Chem. Chem. Phys.*, 2016, **18**, 15510–15513.
- Z.-C. Zeng, S.-C. Huang, D.-Y. Wu, L.-Y. Meng, M.-H. Li, T.-X. Huang, J.-H. Zhong, X. Wang, Z.-L. Yang and B. Ren, *J. Am. Chem. Soc.*, 2015, **137**, 11928–11931.
- D. Korouski, M. Mattei and R. P. Van Duyne, *Nano Lett.*, 2015, **15**, 7956–7962.
- X. Wang, J.-H. Zhong, M. Zhang, Z. Liu, D.-Y. Wu and B. Ren, *Anal. Chem.*, 2015, **88**, 915–921.
- T. Touzalin, S. Joiret, E. Maisonhaute and I. T. Lucas, *Anal. Chem.*, 2017, **89**, 8974–8980.
- M. Mattei, G. Kang, G. Goubert, D. V. Chulhai, G. C. Schatz, L. Jensen and R. P. Van Duyne, *Nano Lett.*, 2016, **17**, 590–596.
- D. Mattox, *Thin Solid Films*, 1973, **18**, 173–186.
- M. George, W. Glaunsinger, T. Thundat and S. Lindsay, *Thin Solid Films*, 1990, **189**, 59–72.
- R. Nyquist, C. Putzig, M. Leugers, R. McLachlan and B. Thill, *Appl. Spectrosc.*, 1992, **46**, 981–987.
- N. Kumar, A. Rae and D. Roy, *Appl. Phys. Lett.*, 2014, **104**, 123106.
- F. Benz, C. Tserkezis, L. O. Herrmann, B. De Nijs, A. Sanders, D. O. Sigle, L. Pukenas, S. D. Evans, J. Aizpurua and J. J. Baumberg, *Nano Lett.*, 2014, **15**, 669–674.
- J. Kalbacova, R. D. Rodriguez, V. Desale, M. Schneider, I. Amin, R. Jordan and D. R. Zahn, *Nanospectroscopy*, 2014, **1**, 12–18.
- W. Zhang, T. Schmid, B.-S. Yeo and R. Zenobi, *J. Phys. Chem. C*, 2008, **112**, 2104–2108.
- R. L. Sobocinski and J. E. Pemberton, *Langmuir*, 1988, **4**, 836–845.
- H. Liu, Y. Sun, Z. Jin, L. Yang and J. Liu, *Chem. Sci.*, 2013, **4**, 3490–3496.
- S. Berweger and M. B. Raschke, *Anal. Bioanal. Chem.*, 2010, **396**, 1613–1613.

- 50 C. F. Bohren and E. E. Clothiaux, *Fundamentals of atmospheric radiation: an introduction with 400 problems*, John Wiley & Sons, 2006.
- 51 J. J. Mock, D. R. Smith and S. Schultz, *Nano Lett.*, 2003, **3**, 485–491.
- 52 M. M. Miller and A. A. Lazarides, *J. Phys. Chem. B*, 2005, **109**, 21556–21565.
- 53 K. L. Kelly, E. Coronado, L. L. Zhao and G. C. Schatz, *J. Phys. Chem. B*, 2003, **107**, 668–677.
- 54 A. Hartschuh, E. J. Sanchez, X. S. Xie and L. Novotny, *Phys. Rev. Lett.*, 2003, **90**, 095503.
- 55 A. Weber-Bargioni, A. Schwartzberg, M. Cornaglia, A. Ismach, J. J. Urban, Y. Pang, R. Gordon, J. Bokor, M. B. Salmeron, D. F. Ogletree, P. Ashby, S. Cabrini and P. J. Schuck, *Nano Lett.*, 2011, **11**, 1201–1207.
- 56 D. Roy and C. Williams, *J. Vac. Sci. Technol., A*, 2010, **28**, 472–475.
- 57 D. Roy, J. Wang and C. Williams, *J. Appl. Phys.*, 2009, **105**, 013530.
- 58 T.-a. Yano, P. Verma, Y. Saito, T. Ichimura and S. Kawata, *Nat. Photonics*, 2009, **3**, 473–477.